J. Fluid Mech. (2015), *vol.* 766, *pp.* 326–336.
doi:10.1017/jfm.2015.25

Measurement of the dispersion relation for random surface gravity waves

Tore Magnus A. Taklo[1], Karsten Trulsen[1,†], Odin Gramstad[1,2], Harald E. Krogstad[3] and Atle Jensen[1]

[1]Department of Mathematics, University of Oslo, PO Box 1053 Blindern, NO-0316 Oslo, Norway

[2]Centre for Ocean Engineering Science and Technology, Swinburne University of Technology, Melbourne VIC 3122, Australia

[3]Department of Mathematical Sciences, NTNU, NO-7491 Trondheim, Norway

(Received 10 September 2013; revised 23 September 2014; accepted 9 January 2015)

We report laboratory experiments and numerical simulations of the Zakharov equation, designed to have sufficient resolution in space and time to measure the dispersion relation for random surface gravity waves. The experiments and simulations are carried out for a JONSWAP spectrum and Gaussian spectra of various bandwidths on deep water. It is found that the measured dispersion relation deviates from the linear dispersion relation above the spectral peak when the bandwidth is sufficiently narrow.

Key words: surface gravity waves, waves/free-surface flows

1. Introduction

Linear wave theory is widely used to model, for instance, the response of ocean structures and ships to water surface gravity waves (Goda 2000; Tucker & Pitt 2001) and assumes that the water surface can be modelled as a linear superposition of regular waves satisfying the linear dispersion relation. For waves on deep water the linear dispersion relation is

$$\omega^2 = gk \tag{1.1}$$

where ω is the angular frequency, k is the wavenumber and g is the acceleration due to gravity.

While the energy contribution of linear waves is located in the linear dispersion relation, nonlinearity can cause energy contributions away from this region. We distinguish two types of nonlinearity (Krogstad & Trulsen 2010), namely static nonlinearity due to bound harmonics and dynamic nonlinearity due to resonant and quasi-resonant wave–wave interactions (Tick 1959; Phillips 1960, 1961). For weakly nonlinear waves, the Zakharov integral equation (Zakharov 1968) or the nonlinear Schrödinger (NLS) equation can be used to account for dynamic nonlinearity.

The typical evolution scale for the dynamic nonlinearity is the Benjamin–Feir (BF) timescale,

$$\tau = (\epsilon^2 \omega_p)^{-1}. \tag{1.2}$$

† Email address for correspondence: karstent@math.uio.no

Here the wave steepness is $\epsilon = a_c k_p$. The characteristic amplitude is $a_c = \sqrt{2\langle\eta^2\rangle}$ where η is the surface elevation and $\langle\cdot\rangle$ denotes statistical averaging. The characteristic wavenumber k_p and frequency ω_p are related by the linear dispersion relation (1.1) and will be further specified below.

Wave dispersion has been well described in experiments (Ramamonjiarisoa & Coantic 1976; Lake & Yuen 1978; Masuda, Kuo & Mitsuyasu 1979; Mitsuyasu, Kuo & Masuda 1979; Donelan, Hamilton & Hui 1985) and in field observations (Hara & Karachintsev 2003; Wang & Hwang 2004). Based on the correlation between pairs of wave staffs, Ramamonjiarisoa & Coantic (1976) and Lake & Yuen (1978) found that spectral components above the spectral peak had phase speeds close to that of the spectral peak and that the energy was essentially propagating with the group velocity of the spectral peak. The correlation estimates from these observations were later explained partly by Phillips (1981) as a consequence of dispersion of short waves in the presence of long waves, and partly by Barrick (1986) as a consequence of bound harmonic components. Nevertheless, a common feature of the measurements above is that none of them provided a simultaneous coverage of the BF scale.

Krogstad & Trulsen (2010) carried out unidirectional simulations with the NLS equation and the modified nonlinear Schrödinger (MNLS) equation of Dysthe (1979). The simulations provided a simultaneous coverage of the BF scale in time and space. From wavenumber–frequency spectra obtained from the simulated surfaces they found that dynamic nonlinear evolution causes deviation from the linear dispersion relation (1.1). Krogstad & Trulsen (2010) found that contributions above the spectral peak had larger phase speeds and group velocities than anticipated from linear theory.

The primary goal of the present paper is to confirm the numerical predictions by Krogstad & Trulsen (2010) with laboratory experiments. The secondary goal is to check the predictions by Krogstad & Trulsen (2010) with a more accurate model, the Zakharov integral equation, which does not have a constraint on bandwidth. In addition to the relatively narrow-banded Gaussian spectra employed by Krogstad & Trulsen (2010), the present experiments and simulations also employ Gaussian spectra of broader bandwidth and a JONSWAP spectrum.

In the present experiments dispersion relations are deduced from high-resolution spatiotemporal measurements of wave fields on deep water in a long and narrow wavetank. The measurements are obtained from a synthetic array which provides simultaneous coverage of the BF scale. A presentation of the experimental setup and the measurement technique is given in § 2, the numerical Zakharov model is presented in § 3, and the results are presented in § 4.

2. Experimental setup and measurement technique

2.1. *Wavetank and synthetic array*

The experiments were performed in a long and narrow wavetank at the Department of Mathematics at the University of Oslo. Figure 1 shows a sketch of the wavetank seen from above. It is 0.5 m wide and 24.6 m long. Waves were generated by a hydraulic piston wave maker and propagated towards a damping beach.

We introduce a coordinate system such that x is along the tank, y is across the tank and z is the vertical axis pointing up. The equilibrium position of the wave maker is located at $x = 0$ and the damping beach starts at $x = 21.6$ m. The water depth $h = 0.5$ m was constant from the wave maker to the start of the damping beach.

The surface elevation η was measured with 16 ultrasonic probes. The probes were non-intrusive, vertically looking down and were located at height $H = 6.0$, 12.0 or

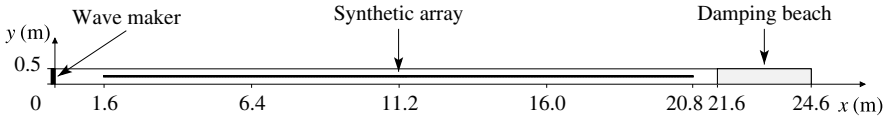

FIGURE 1. Top-view of the wavetank showing actual ratio between width and length.

15.0 cm above mean water level, $z = 0$, in experiments with different wave fields. The beam angle was $\beta = 6°$ and the footprints were respectively $L_\beta = 0.6$, 1.3 or 1.6 cm, computed from β and H. One characteristic wavelength λ_p covered approximately 46, 21 or 17 footprints, respectively.

The probes were combined to form a stationary equispaced array with spatial resolution equal to 30 cm and length 4.8 m. On the top of the wavetank the stationary array was mounted on rails so that it could be moved along the length of the wavetank between the wave maker and the damping beach. The probes and the wave maker were controlled by a computer and synchronized via a data acquisition card with 16 input channels. Dense spatiotemporal measurements were achieved by measuring the surface elevations several times at different locations along the wavetank in different runs of the same wave field. The resulting arrangement of equispaced measurement positions along the wavetank is referred to as a synthetic array.

The synthetic array depends on the wave field being repeatable in the wavetank. The repeatability of the wave fields was tested and the repetition error was estimated from 112 measurement positions between $x = 1.6$ and 20.8 m from the wave maker. The raw data from the probes contained noise and drop-out spikes due to the measurement limitations of the probes. The noise and the drop-out spikes were removed and replaced by cubic interpolations. The repetition error of the wave fields, after interpolation, was on average about 1.3 %.

A synthetic array with $M = 384$ equispaced measurement positions and spatial resolution $\Delta x = 5$ cm was used to measure all wave fields. The synthetic array is shown in figure 1 and had length $L = M\Delta x = 19.2$ m between $x = 1.6$ and 20.8 m from the wave maker.

Whenever we refer to the experiments we let ω_p be the frequency of the peak of the input spectrum to the wave maker, and let the corresponding wavenumber $k_p = \omega_p^2/g$ be determined according to the linear dispersion relation (1.1). The synthetic array covered 70 wavelengths, $L = 70\lambda_p$, for $\lambda_p = 27.4$ cm corresponding to $\omega_p = 15.0$ s^{-1}, $T_p = 0.419$ s and $k_p = 22.9$ m^{-1}. The non-dimensional water depth was $k_p h = 11.5$. The peaks in the experimental wavenumber–frequency spectra in § 4 were not situated exactly at (k_p, ω_p) but close to this point.

The wavenumber axis $k \in [0, 5.46k_p]$ in the experimental wavenumber–frequency spectra in § 4 was discretized with a uniform grid of $M = 384$ discrete modes with $\Delta k/k_p = 2\pi/Lk_p = 0.0143$.

The sampling rate of the probes was 200 Hz and $\Delta t = 0.005$ s. With this choice of sampling rate the probes were able to reconstruct frequencies up to the Nyquist frequency of approximately $42\omega_p$. The wave fields were measured for $T = 400T_p$ and 33 736 time samples were taken from each measurement position. Startup effects were removed and the last $170T_p$ (14 280 time samples) were used for spectral estimates.

The laboratory wave fields were initialized with wave steepness $\epsilon = a_c k_p = 0.10$ where the characteristic amplitude was determined at the first measurement position at $x = 1.6$ m closest to the wave maker. For our choice of ϵ and ω_p the BF timescale is

$\tau \approx 16T_p$ from (1.2) with typical propagation distance $c_g\tau = 2.18$ m; thus the synthetic array covers the BF scale.

We observed significant attenuation of the wave fields along the wavetank in the experiments. This can have three causes: the first is the development of transverse modes which have a node at the centreline where we took measurements, see Trulsen, Stansberg & Velarde (1999); the second is viscous dissipation; and the third is wave breaking. Sporadic wave breaking was observed in the experiments. We carried out an analysis of the viscous dissipation in the wavetank. The spatial decay rates of the wave fields compared well with established models (Lamb 1932; Hunt 1952; Van Dorn 1966). For this reason we anticipate that spreading due to transverse modes (Trulsen *et al.* 1999) and wave breaking is not important in our experiments.

2.2. *Input spectrum for experiments*

Random wave fields were mechanically generated at the wave maker. The random phases were uniformly distributed on the interval $[0, 2\pi)$ and the amplitudes were determined from a Gaussian spectrum,

$$S(\omega) = \frac{H_s^2}{16\sigma_t\omega_p\sqrt{2\pi}} \exp\left[-\frac{1}{2}\left(\frac{\omega-\omega_p}{\sigma_t\omega_p}\right)^2\right], \tag{2.1}$$

or a JONSWAP spectrum,

$$S(\omega) = \frac{\alpha g^2}{\omega^5} \exp\left[-\frac{5}{4}\left(\frac{\omega_p}{\omega}\right)^4\right] \gamma^{\exp\left[(-(\omega-\omega_p)^2/2\sigma^2\omega_p^2)\right]}. \tag{2.2}$$

For the Gaussian input spectrum σ_t is the width and H_s is the significant wave height. For the JONSWAP spectrum the peak enhancement factor is $\gamma = 3.3$, α is the Phillips factor and

$$\sigma = \begin{cases} 0.07, & \omega \leqslant \omega_p \\ 0.09, & \omega > \omega_p. \end{cases} \tag{2.3}$$

The experimental wave fields are summarized in table 1: six Gaussian spectra denoted Gaussian 1–6, with σ_t and ϵ as indicated, and one JONSWAP spectrum. The meaning of the third column in table 1 is explained in § 3.

Figures 2 and 3 show the feedback spectra of the actual wave maker motion and the frequency spectra measured at the probe closest to the wave maker with logarithmic vertical axis for the Gaussian wave fields and the JONSWAP wave field, respectively. The measured spectra were obtained from the last $170T_p$ of the time series measured at the probe closest to the wave maker. The measured spectra were smoothed by Welch's method. The time series of $170T_p$ were divided into nine sections and the sections were windowed with Hamming windows and overlapped by 50 %. Each section covered approximately $19T_p$. Both the feedback spectra and the measured spectra are denoted S and are normalized relative to their respective peak values S_p. The feedback and measured spectra agree well around the spectral peak.

3. Numerical simulations

3.1. *Zakharov integral equation*

Our simulations were performed using a numerical implementation of the Zakharov (1968) equation. The Zakharov equation describes the weakly nonlinear evolution of

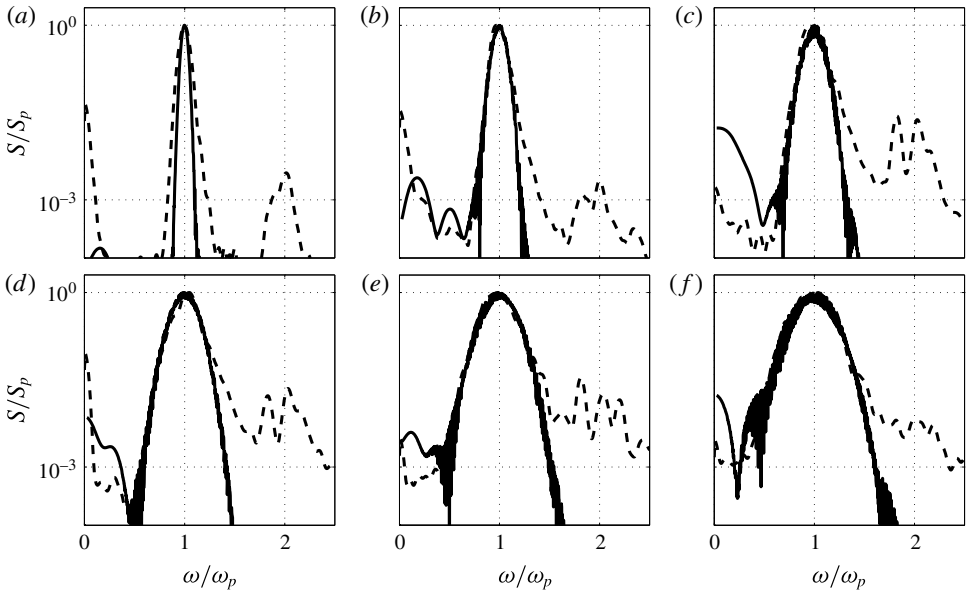

FIGURE 2. Feedback spectra of the actual wave maker motion (——). Frequency spectra measured at the probe closest to the wave maker (– – –): (*a–f*) Gaussian 1–6.

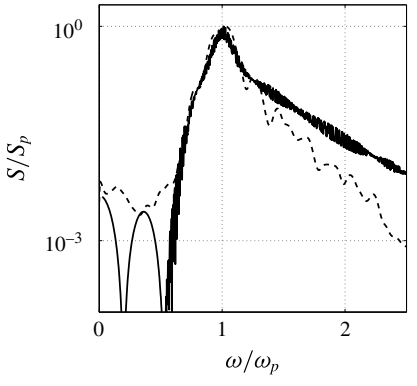

FIGURE 3. JONSWAP feedback spectrum of the actual wave maker motion (——). JONSWAP frequency spectrum measured at the probe closest to the wave maker (- - - -).

the generalized complex amplitude $b(\boldsymbol{k}, t)$ and has the form

$$\mathrm{i}\frac{\partial b(\boldsymbol{k})}{\partial t} = \omega(\boldsymbol{k})b(\boldsymbol{k}) + \int T(\boldsymbol{k}, \boldsymbol{k}_1, \boldsymbol{k}_2, \boldsymbol{k}_3)b^*(\boldsymbol{k}_1)b(\boldsymbol{k}_2)b(\boldsymbol{k}_3)\delta(\boldsymbol{k}+\boldsymbol{k}_1-\boldsymbol{k}_2-\boldsymbol{k}_3)\mathrm{d}\boldsymbol{k}_1\mathrm{d}\boldsymbol{k}_2\mathrm{d}\boldsymbol{k}_3. \tag{3.1}$$

Here t is time, $\boldsymbol{k}$ is the wavenumber vector and $\omega(\boldsymbol{k}) = \sqrt{g|\boldsymbol{k}|\tanh(|\boldsymbol{k}|h)}$ is the angular frequency, where g is the acceleration due to gravity and h is the water depth, and the asterisk denotes complex conjugation. The kernel function $T(\boldsymbol{k}, \boldsymbol{k}_1, \boldsymbol{k}_2, \boldsymbol{k}_3)$ is a complicated function describing all the nonlinear interactions between the wave components. Details about $T(\boldsymbol{k}, \boldsymbol{k}_1, \boldsymbol{k}_2, \boldsymbol{k}_3)$ can be found in e.g. Krasitskii (1994).

Wave field	σ_t	ϵ	σ_x
Gaussian 1	0.03	0.10	0.05
Gaussian 2	0.06	0.10	0.11
Gaussian 3	0.08	0.10	0.17
Gaussian 4	0.11	0.10	0.22
Gaussian 5	0.14	0.10	0.28
Gaussian 6	0.17	0.10	0.33
JONSWAP	—	0.10	—

TABLE 1. Dimensionless parameters used for the experiments and simulations with the Gaussian spectra and the JONSWAP spectrum: σ_t, width of input frequency spectrum to the wave maker in the experiments; ϵ, wave steepness at the probe closest to the wave maker in the experiments; and σ_x, width of initial wavenumber spectrum for the simulations.

The complex amplitude $b(\boldsymbol{k}, t)$ only contains the free-wave components of the wave field. That is, bound-wave components, arising as a result of non-resonant nonlinear interactions, are not contained in $b(\boldsymbol{k}, t)$, but can be reconstructed from $b(\boldsymbol{k}, t)$ as an integral power series in the form

$$\begin{aligned} a(\boldsymbol{k}) \;=\; & b(\boldsymbol{k}) + \int A^{(1)}(\boldsymbol{k}, \boldsymbol{k}_1, \boldsymbol{k}_2) b(\boldsymbol{k}_1) b(\boldsymbol{k}_2) \delta(\boldsymbol{k} - \boldsymbol{k}_1 - \boldsymbol{k}_2) \mathrm{d}\boldsymbol{k}_1 \mathrm{d}\boldsymbol{k}_2 \\ & + \int A^{(2)}(\boldsymbol{k}, \boldsymbol{k}_1, \boldsymbol{k}_2) b^*(\boldsymbol{k}_1) b(\boldsymbol{k}_2) \delta(\boldsymbol{k} + \boldsymbol{k}_1 - \boldsymbol{k}_2) \mathrm{d}\boldsymbol{k}_1 \mathrm{d}\boldsymbol{k}_2 \\ & + \int A^{(3)}(\boldsymbol{k}, \boldsymbol{k}_1, \boldsymbol{k}_2) b^*(\boldsymbol{k}_1) b^*(\boldsymbol{k}_2) \delta(\boldsymbol{k} + \boldsymbol{k}_1 + \boldsymbol{k}_2) \mathrm{d}\boldsymbol{k}_1 \mathrm{d}\boldsymbol{k}_2 \\ & + \text{third-order terms}. \end{aligned} \tag{3.2}$$

The kernel functions appearing in (3.2) can be found in Krasitskii (1994). From $a(\boldsymbol{k})$, the surface elevation $\eta(\boldsymbol{x}, t)$, including both free and bound harmonics, can be found as

$$\eta(\boldsymbol{x}, t) = \frac{1}{2\pi} \int \left(\frac{\omega(\boldsymbol{k})}{2g} \right)^{1/2} a(\boldsymbol{k}) \mathrm{e}^{\mathrm{i}\boldsymbol{k}\cdot\boldsymbol{x}} \mathrm{d}\boldsymbol{k} + *. \tag{3.3}$$

In order to solve the Zakharov equation numerically we have employed a discrete representation of the wavenumber plane, i.e.

$$b(\boldsymbol{k}, t) = \sum_n b_n(t) \delta(\boldsymbol{k} - \boldsymbol{k}_n). \tag{3.4}$$

For the discrete spectrum (3.4), the Zakharov equation is replaced by the system of ordinary differential equations

$$\frac{\mathrm{d}b_n}{\mathrm{d}t} = -\mathrm{i}\omega_n b_n - \mathrm{i} \sum_{m,q,r} T_{nmqr} b_m^* b_q b_r \delta_{n+m-q-r}, \tag{3.5}$$

where $T_{nmqr} = T(\boldsymbol{k}_n, \boldsymbol{k}_m, \boldsymbol{k}_q, \boldsymbol{k}_r)$, $\omega_n = \omega(\boldsymbol{k}_n)$ and $\delta_{n+m-q-r}$ is the Kronecker delta

$$\delta_{n+m-q-r} = \begin{cases} 1, & \text{when } \boldsymbol{k}_n + \boldsymbol{k}_m = \boldsymbol{k}_q + \boldsymbol{k}_r, \\ 0, & \text{otherwise.} \end{cases} \tag{3.6}$$

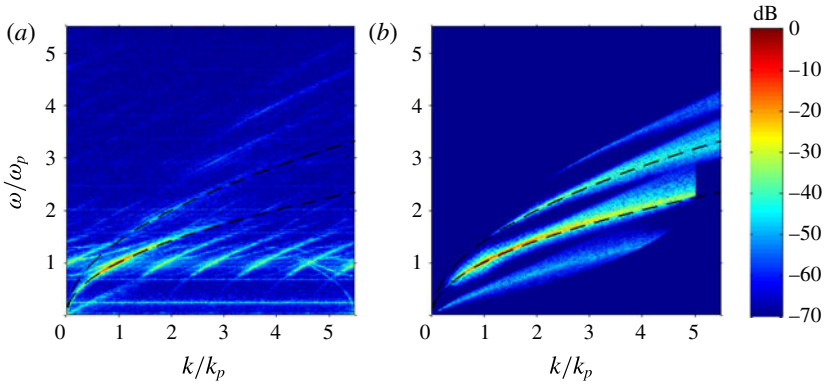

FIGURE 4. Wavenumber–frequency spectra from experiment (*a*) and simulation (*b*) with the JONSWAP wave field. Colour scale in dB relative to the peak. Lower dashed curve, linear dispersion relation; upper dashed curve, second-harmonic dispersion shell.

3.2. *Initial spectrum for simulations*

Corresponding to the seven experiments, Gaussian 1–6 and JONSWAP, we carried out numerical simulations using a Gaussian wavenumber spectrum,

$$S(k) = \frac{\epsilon^2}{\sigma_x\sqrt{2\pi}} \exp\left[-\frac{(k/k_p - 1)^2}{2\sigma_x^2}\right], \tag{3.7}$$

and a standard JONSWAP wavenumber spectrum, see equation (4.8a) in Gramstad & Stiassnie (2013). The widths σ_x chosen for the numerical simulations are listed in the third column in table 1.

Whenever we refer to the simulations we let k_p be the wavenumber of the spectral peak of the initial spectrum for the simulations and let $\omega_p = \sqrt{gk_p}$ according to the linear dispersion relation (1.1). In all simulations the wave steepness was set to $\epsilon = 0.10$, which was the same as the measured steepness at the measurement position closest to the wave maker in the experiments. However, due to dissipation in the wavetank, the steepness in the numerical simulations was larger than in the experiments after some propagation distance.

Wavenumbers in the interval $k \in [0,\ 5.5k_p]$ were discretized by a regular grid with 256 discrete modes. The simulations were run up to $T = 152T_p$, where the first $12T_p$ of the evolution was not used when calculating the spectra. Considering the group velocity of the waves, the choice of simulation time was inspired by the experiments, where a total evolution distance $L = 70\lambda_p$ was captured and where the first measurement position was located at approximately $6\lambda_p$. From the numerical solution for $b_n(t)$, the bound harmonics were found up to third order according to (3.2), and then the surface elevation $\eta(\boldsymbol{x}, t)$ was found from the discrete version of (3.3).

4. Experimental and numerical results

Wavenumber–frequency spectra were obtained from two-dimensional discrete Fourier transform in space and time of measured or simulated surface elevation. The colours in the subsequent contour plots show the spectral energy density in decibels (dB) relative to the peak. In figures 4–6 the lower dashed curve is the

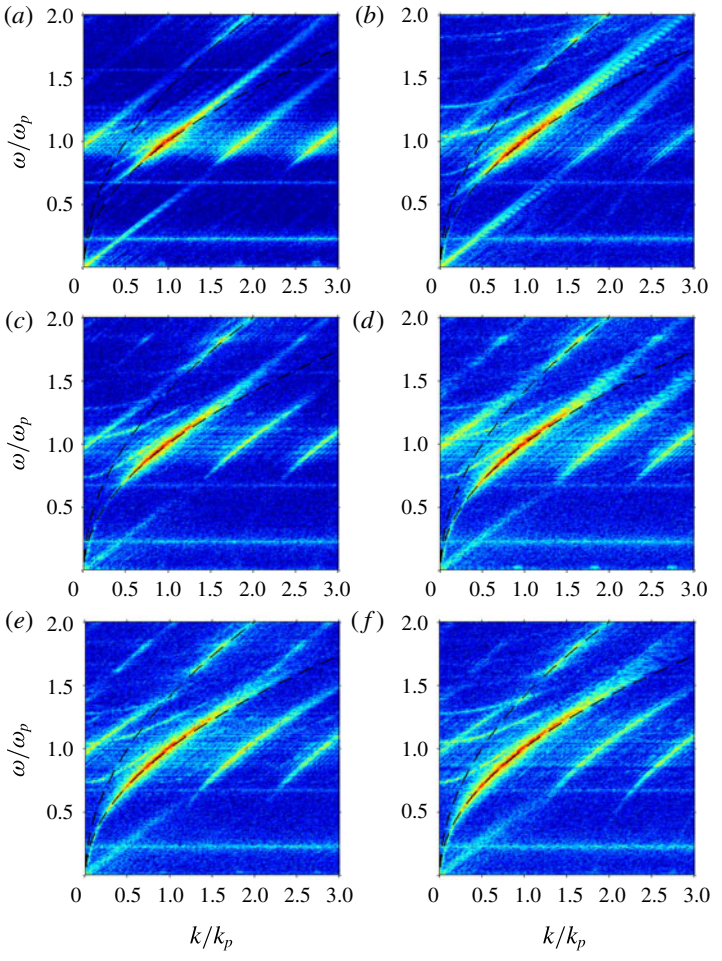

FIGURE 5. Wavenumber–frequency spectra of Gaussian 1–6, (*a–f*), from experiments. Colour scale as in figure 4. Lower dashed curve, linear dispersion relation; upper dashed curve, second-harmonic dispersion shell.

linear dispersion relation (k, ω) and the upper dashed curve is the second-harmonic dispersion shell $(2k, 2\omega)$, with $\omega = \sqrt{gk}$.

Figure 4 shows the wavenumber–frequency spectra from the experiment and simulation with the JONSWAP wave field. The measured dispersion relation suggests the validity of the linear dispersion relation. In the spectrum from this experiment we observe the zeroth harmonic at the bottom left and higher harmonics up to the fifth harmonic at the top right.

Energy is also seen extending up to the left from the lower right corner of the spectrum from the experiment. This distribution corresponds to reflected waves from the damping beach appearing here at high wavenumbers due to aliasing; it belongs to the negative wavenumber axis adjacent to the origin. We also performed experiments where the damping beach was substituted with a vertical wall, showing a significant increase of reflected wave energy. In order to show the higher-harmonic dispersion shells we present the JONSWAP spectrum with only positive wavenumbers.

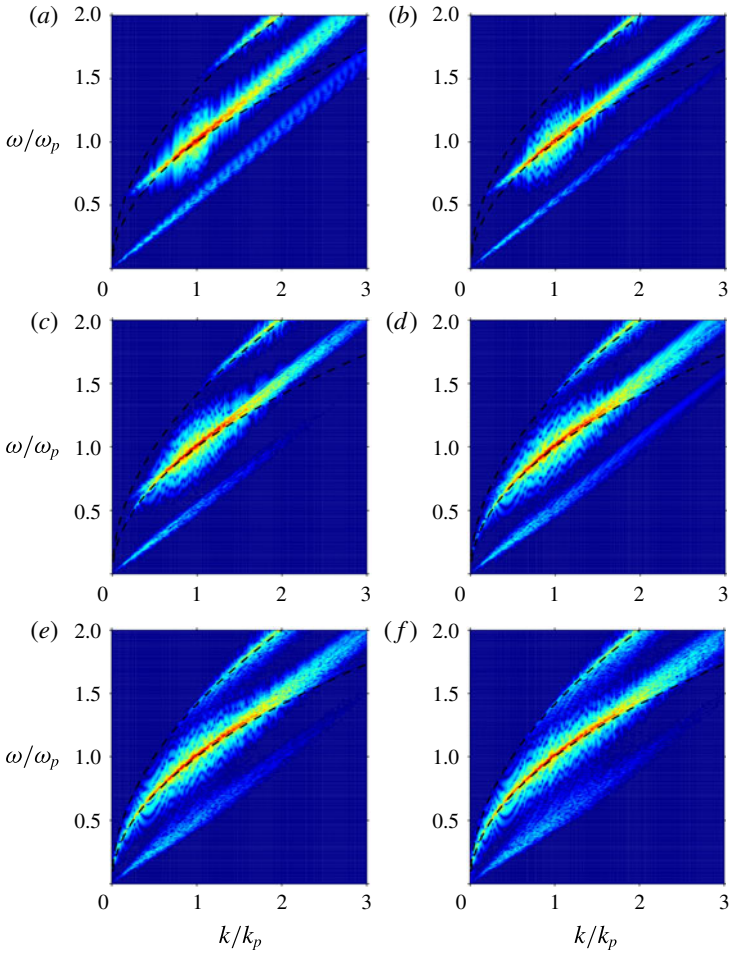

FIGURE 6. Wavenumber–frequency spectra of Gaussian 1–6, (*a–f*), from simulations. Colour scale as in figure 4. Lower dashed curve, linear dispersion relation; upper dashed curve, second-harmonic dispersion shell.

In the spectrum from the experiments diagonal distributions parallel and similar to the peak distribution are observed. The peak distribution is centred at k_p while adjacent diagonal distributions are centred at approximately $0.1k_p$, $1.9k_p$, $2.8k_p$, $3.7k_p$ and $4.6k_p$. The distance between neighbouring distributions is $0.9k_p$, which corresponds to $2\pi/0.9k_p \approx 30.5$ cm. This agrees well with the distance between the probes in the stationary array, which is 30 cm; thus these distributions may be an artifact of our measuring technique.

Figure 5 shows the wavenumber–frequency spectra of Gaussian 1–6 from the experiments. In order to focus on the deviation from the linear dispersion relation we observe the spectra closer to the peak than in figure 4. The measured dispersion relation suggests that the linear dispersion relation is not fully satisfied when the bandwidth is sufficiently narrow. For the wave fields with the narrowest bandwiths, Gaussian 1 and 2, the leading-order wave energy is distributed tangentially to the linear dispersion relation at the peak. The observation suggests that spectral components above peak can have larger phase speeds than those anticipated by linear

theory and that spectral components above peak tend to have group velocities similar to that of the peak. The experiments of Gaussian 1 and 2 confirm the numerical predictions of the (M)NLS equations by Krogstad & Trulsen (2010).

For the broad-banded wave fields, Gaussian 5 and 6, the measured dispersion relation agrees well with the linear dispersion relation. For Gaussian 3 and 4 the deviation is less than for Gaussian 1 and 2, which indicates that the deviation varies with bandwidth for a fixed steepness. In all Gaussian wavenumber–frequency spectra from the experiments bound harmonics were identified up to fifth order and the zeroth harmonic can be seen below peak in all spectra.

Horizontal distributions at angular frequencies of $\omega/\omega_p = 0.2$ and 0.7 are also seen in the spectra from the experiments. We have no explanation for these; they do not have the same frequencies as seiche modes in the wavetank. The longest longitudinal seiche mode in the wavetank has angular frequency $\omega/\omega_p = 0.02$ and the ninth mode has angular frequency $\omega/\omega_p = 0.30$.

Figure 6 shows the wavenumber–frequency spectra of Gaussian 1–6 from the simulations of the Zakharov integral equation. For the narrow-banded wave fields the simulations validate the results from the (M)NLS equations by Krogstad & Trulsen (2010). As for the experiments the broad-banded wave fields agree well with linear theory. The variation in the deviation for various bandwidths and fixed steepness is also observed from the simulations of the Zakharov equation.

5. Conclusion

We have performed laboratory experiments designed to have sufficient resolution in space and time to measure the dispersion relation for random surface gravity waves and confirmed the numerical predictions of the (M)NLS equations by Krogstad & Trulsen (2010). A more accurate model than the (M)NLS equations, the Zakharov integral equation, validates the simulations by Krogstad & Trulsen (2010). For a JONSWAP spectrum and Gaussian spectra of various bandwidths we find that the measured dispersion relation deviates from the linear dispersion relation above the spectral peak when the bandwidth is sufficiently narrow. For the broad-banded spectra the measured dispersion relation agrees well with linear wave theory.

Acknowledgements

This research has been supported by the University of Oslo and the Research Council of Norway through grant 214556/F20. We thank S. Vesterby for assistance with the setup of the laboratory array and J. C. Nieto Borge for valuable discussions.

REFERENCES

BARRICK, E. 1986 The role of the gravity-wave dispersion relation in HF radar measurements of the sea surface. *IEEE J. Ocean. Engng* **11**, 286–292.

DONELAN, M. A., HAMILTON, J. & HUI, W. H. 1985 Directional spectra of wind-generated waves. *Phil. Trans. R. Soc. Lond.* A **315**, 509–562.

DYSTHE, K. B. 1979 Note on a modification to the nonlinear Schrödinger equation for application to deep water waves. *Phil. Trans. R. Soc. Lond.* A **369**, 105–114.

GODA, Y. 2000 *Random Seas and Design of Maritime Structures*. World Scientific.

GRAMSTAD, O. & STIASSNIE, M. 2013 Phase-averaged equation for water waves. *J. Fluid Mech.* **718**, 280–303.

HARA, T. & KARACHINTSEV, A. V. 2003 Observation of nonlinear effects in ocean surface wave frequency spectra. *J. Phys. Oceanogr.* **33**, 422–430.

HUNT, J. N. 1952 Viscous damping waves over an inclined bed in a channel of finite width. *La Houille Blanche* **6**, 836–841.

KRASITSKII, V. P. 1994 On reduced equations in the Hamiltonian theory of weakly nonlinear surface-waves. *J. Fluid Mech.* **272**, 1–20.

KROGSTAD, H. E. & TRULSEN, K. 2010 Interpretations and observations of ocean wave spectra. *Ocean Dyn.* **60**, 973–991.

LAKE, B. M. & YUEN, H. C. 1978 A new model for nonlinear wind waves. Part 1. Physical model and experimental evidence. *J. Fluid Mech.* **88**, 33–62.

LAMB, H. 1932 *Hydrodynamics*, 6th edn. Dover.

MASUDA, A., KUO, Y. Y. & MITSUYASU, H. 1979 On the dispersion relation of random gravity waves. Part 1. Theoretical framework. *J. Fluid Mech.* **92**, 717–730.

MITSUYASU, H., KUO, Y. Y. & MASUDA, A. 1979 On the dispersion relation of random gravity waves. Part 2. An experiment. *J. Fluid Mech.* **92**, 731–749.

PHILLIPS, O. M. 1960 On the dynamics of unsteady gravity waves of finite amplitude. Part 1. *J. Fluid Mech.* **9**, 193–217.

PHILLIPS, O. M. 1961 On the dynamics of unsteady gravity waves of finite amplitude. Part 2. *J. Fluid Mech.* **11**, 143–155.

PHILLIPS, O. M. 1981 The dispersion of short wavelets in the presence of a dominant long wave. *J. Fluid Mech.* **107**, 456–485.

RAMAMONJIARISOA, A. & COANTIC, M. 1976 Loi expérimental de dispersion des vagues produites par le vent sur une faible longueur d'action. *C. R. Acad. Sci. Paris* B **282**, 111–113.

TICK, L. J. 1959 A nonlinear random model of gravity waves. Part 1. *J. Math. Mech.* **8**, 643–651.

TRULSEN, K., STANSBERG, C. T. & VELARDE, M. G. 1999 Laboratory evidence of three-dimensional frequency downshift of waves in a long tank. *Phys. Fluids* **11**, 235–237.

TUCKER, M. J. & PITT, E. G. 2001 *Waves in Ocean Engineering*. Elsevier Science & Technology.

VAN DORN, W. G. 1966 Boundary dissipation of oscillatory waves. *J. Fluid Mech.* **24**, 769–779.

WANG, D. W. & HWANG, P. A. 2004 The dispersion relation of short wind waves from space–time wave measurement. *J. Atmos. Ocean. Technol.* **21**, 1936–1945.

ZAKHAROV, V. E. 1968 Stability of periodic waves of finite amplitude on the surface of a deep fluid. *J. Appl. Mech. Tech. Phys.* **9**, 190–194.